

Plug-and-Play ADMM for Image Restoration: Fixed Point Convergence and Applications

Stanley H. Chan, *Member, IEEE*, Xiran Wang, *Student Member, IEEE*, Omar A. Elgendy, *Student Member, IEEE*

Abstract—Alternating direction method of multiplier (ADMM) is a widely used algorithm for solving constrained optimization problems in image restoration. Among many useful features, one critical feature of the ADMM algorithm is its *modular structure* which allows one to plug in any off-the-shelf image denoising algorithm for a subproblem in the ADMM algorithm. Because of the plug-in nature, this type of ADMM algorithms is coined the name “Plug-and-Play ADMM”. Plug-and-Play ADMM has demonstrated promising empirical results in a number of recent papers. However, it is unclear under what conditions and for what denoising algorithms would it guarantee convergence. Also, it is unclear to what extent would Plug-and-Play ADMM be compared to existing methods for common Gaussian and Poissonian image restoration problems.

In this paper, we propose a Plug-and-Play ADMM algorithm with provable fixed point convergence. We show that for any denoising algorithm satisfying a boundedness criteria, called *bounded denoisers*, Plug-and-Play ADMM converges to a fixed point under a continuation scheme. We demonstrate applications of Plug-and-Play ADMM on two image restoration problems including single image super-resolution and quantized Poisson image recovery for single-photon imaging. We compare Plug-and-Play ADMM with state-of-the-art algorithms in each problem type, and demonstrate promising experimental results of the algorithm.

Index Terms—ADMM, Plug-and-Play, image restoration, denoising, deblurring, inpainting, super-resolution, Poisson noise.

I. INTRODUCTION

A. ADMM

Many image restoration tasks can be posed as the following inverse problem: Given an observed image $\mathbf{y} \in \mathbb{R}^n$ possibly corrupted according to some forward model and noise, find the underlying image $\mathbf{x} \in \mathbb{R}^n$ which “best explains” the observation. In estimation, we often formulate this problem as a maximum-a-posteriori (MAP) estimation [1], where the goal is to maximize the posterior probability:

$$\begin{aligned} \hat{\mathbf{x}} &= \operatorname{argmax}_{\mathbf{x}} p(\mathbf{x} | \mathbf{y}) \\ &= \operatorname{argmin}_{\mathbf{x}} -\log p(\mathbf{y} | \mathbf{x}) - \log p(\mathbf{x}), \end{aligned} \quad (1)$$

for some conditional probability $p(\mathbf{y} | \mathbf{x})$ defining the forward imaging model, and a prior distribution $p(\mathbf{x})$ defining the probability distribution of the latent image. Because of the explicit use of the forward and the prior models, MAP estimation is

The authors are with the School of Electrical and Computer Engineering, Purdue University, West Lafayette, IN 47907, USA. S. Chan is also with the Department of Statistics, Purdue University, West Lafayette, IN 47907, USA. Emails: {stanleychan, wang470, oelgendy}@purdue.edu.

This paper follows the concept of reproducible research. All the results and examples presented in the paper are reproducible using the code and images available online at <http://engineering.purdue.edu/ChanGroup/>.

also a model-based image reconstruction (MBIR) method [2] which has many important applications in deblurring [3]–[5], interpolation [6]–[8], super-resolution [9]–[12] and computed tomography [13], to name a few.

It is not difficult to see that solving the MAP problem in (1) is equivalent to solving an optimization problem

$$\hat{\mathbf{x}} = \operatorname{argmin}_{\mathbf{x}} f(\mathbf{x}) + \lambda g(\mathbf{x}), \quad (2)$$

with $f(\mathbf{x}) \stackrel{\text{def}}{=} -\log p(\mathbf{y} | \mathbf{x})$ and $g(\mathbf{x}) \stackrel{\text{def}}{=} -(1/\lambda) \log p(\mathbf{x})$. The optimization in (2) is a generic unconstrained optimization. This suggests that many standard optimization algorithms can be used to solve the problem. In this paper, we will primarily focus on the alternating direction method of multiplier (ADMM) [14], which has become the workhorse for a variety of problems in the form of (2).

The idea of ADMM is to convert the unconstrained optimization in (2) into a constrained problem

$$(\hat{\mathbf{x}}, \hat{\mathbf{v}}) = \operatorname{argmin}_{\mathbf{x}, \mathbf{v}} f(\mathbf{x}) + \lambda g(\mathbf{v}), \quad \text{subject to } \mathbf{x} = \mathbf{v}, \quad (3)$$

and consider the augmented Lagrangian function of (3):

$$\mathcal{L}(\mathbf{x}, \mathbf{v}, \mathbf{u}) = f(\mathbf{x}) + \lambda g(\mathbf{v}) + \mathbf{u}^T (\mathbf{x} - \mathbf{v}) + \frac{\rho}{2} \|\mathbf{x} - \mathbf{v}\|^2. \quad (4)$$

Then, the solution is found by seeking a saddle point of \mathcal{L} , which involves solving a sequence of subproblems in the form

$$\mathbf{x}^{(k+1)} = \operatorname{argmin}_{\mathbf{x} \in \mathbb{R}^n} f(\mathbf{x}) + \frac{\rho}{2} \|\mathbf{x} - \tilde{\mathbf{x}}^{(k)}\|^2, \quad (5)$$

$$\mathbf{v}^{(k+1)} = \operatorname{argmin}_{\mathbf{v} \in \mathbb{R}^n} \lambda g(\mathbf{v}) + \frac{\rho}{2} \|\mathbf{v} - \tilde{\mathbf{v}}^{(k)}\|^2, \quad (6)$$

$$\bar{\mathbf{u}}^{(k+1)} = \bar{\mathbf{u}}^{(k)} + (\mathbf{x}^{(k+1)} - \mathbf{v}^{(k+1)}), \quad (7)$$

where $\bar{\mathbf{u}}^{(k)} \stackrel{\text{def}}{=} (1/\rho)\mathbf{u}^{(k)}$ is the scaled multiplier, $\tilde{\mathbf{x}}^{(k)} \stackrel{\text{def}}{=} \mathbf{x}^{(k)} - \bar{\mathbf{u}}^{(k)}$ and $\tilde{\mathbf{v}}^{(k)} \stackrel{\text{def}}{=} \mathbf{v}^{(k+1)} + \bar{\mathbf{u}}^{(k)}$. Under mild conditions, e.g., when both f and g are closed, proper and convex, and if a saddle point of \mathcal{L} exists, one can show that the iterates returned by (5)-(7) converges to the solution of (3) (See [14] for details).

B. Plug-and-Play ADMM

An important feature of the ADMM iterations (5)-(7) is its modular structure. In particular, (5) can be regarded as an inversion step as it involves the forward imaging model $f(\mathbf{x})$, whereas (6) can be regarded as a denoising step as it involves the prior $g(\mathbf{v})$. To see the latter, if we define $\sigma = \sqrt{\lambda/\rho}$, it is not difficult to show that (6) is

$$\mathbf{v}^{(k+1)} = \operatorname{argmin}_{\mathbf{v} \in \mathbb{R}^n} g(\mathbf{v}) + \frac{1}{2\sigma^2} \|\mathbf{v} - \tilde{\mathbf{v}}^{(k)}\|^2. \quad (8)$$

Treating $\tilde{v}^{(k)}$ as the “noisy” image, (8) minimizes the residue between $\tilde{v}^{(k)}$ and the “clean” image v using the prior $g(v)$. For example, if $g(x) = \|x\|_{TV}$ (the total variation norm), then (8) is the standard total variation denoising problem.

Building upon this intuition, Venkatakrishnan et al. [15] proposed a variant of the ADMM algorithm by suggesting that one does not need to specify g before running the ADMM. Instead, one can replace (6) using an off-the-shelf image denoising algorithm, denoted by \mathcal{D}_σ , to yield

$$v^{(k+1)} = \mathcal{D}_\sigma(\tilde{v}^{(k)}). \quad (9)$$

Because of the heuristic nature of the method, they called the resulting algorithm as the Plug-and-Play ADMM. An interesting observation they found in [15] is that although Plug-and-Play ADMM appears ad-hoc, for a number of image reconstruction problems the algorithm indeed performs better than many state-of-the-art methods. A few recent reports have concurred similar observations [13], [16], [17].

C. Challenges of Plug-and-Play ADMM

From a theoretical point of view, the main challenge of analyzing Plug-and-Play ADMM is the denoiser \mathcal{D}_σ . Since \mathcal{D}_σ is often nonlinear and does not have closed form expressions, it has been very difficult to analyze the behavior of the Plug-and-Play ADMM. Specifically, the following three questions remain open:

- 1) Convergence of the Algorithm. Classical results of ADMM require g to be closed, proper and convex in order to ensure convergence [14]. While newer results have extended ADMM for nonconvex problems [18], there is little work addressing the case when g is defined implicitly through \mathcal{D}_σ . To the best of our knowledge, the only existing convergence analysis, to date, is the one by Sreehari et al. [13] for the case when \mathcal{D}_σ is a symmetric smoothing filter [19], [20]. However, for general \mathcal{D}_σ the convergence is not known.
- 2) Original Prior. Since \mathcal{D}_σ is an off-the-shelf image denoising algorithm, it is unclear what prior g does it correspond to. In [21], Chan addresses this question by explicitly deriving the original prior g when \mathcal{D}_σ is a symmetric smoothing filter [21]. In this case, the author shows that g is a modified graph Laplacian prior, with better restoration performance compared to the conventional graph Laplacian [22]. However, beyond symmetric smoothing filters it becomes unclear if we can find the corresponding g .
- 3) Implementation. The usage of Plug-and-Play ADMM has been reported in a few scattered occasions, with some work in electron tomography [13], compressive sensing [16], and some very recent applications in Poisson recovery [17]. However, the common challenge underpinning these applications is whether one can obtain a fast solver for the inversion step in (5). This has not been a problem for conventional ADMM, because in many cases we can use another variable splitting strategy to replace $v = x$ in (3), e.g., $v = Bx$ when $g(x) = \|Bx\|_1$.

D. Related Works

Plug-and-Play ADMM was first reported in 2013. Around the same period of time there is an independent series of studies using denoisers for approximate message passing (AMP) algorithms [23]–[26]. The idea was to replace the shrinkage step of the standard AMP algorithm with any off-the-shelf algorithm in the class of “proper denoisers” – denoisers which ensure that the noise variance is sufficiently suppressed. (See Section II-C for more discussions.) However, this type of denoise-AMP algorithms rely heavily on the Gaussian statistics of the random measurement matrix A in a specific forward model $f(x) = \|Ax - y\|^2$. Thus, if $f(x)$ departs from quadratic or A is not random, then the behavior of the denoise-AMP becomes unclear.

Using denoisers as building blocks of an image restoration algorithm can be traced back further, e.g., a wavelet denoiser for signal deconvolution [27]. Of particular relevance to Plug-and-Play ADMM is the work of Danielyan et al. [28], where they proposed a variational method for deblurring using BM3D as a prior. The idea was later developed by Zhang et al. to other restoration problems [29]. However, these algorithms are customized for a specific denoiser. In contrast, the proposed Plug-and-Play ADMM supports any denoiser satisfying appropriate assumptions. Another difference is that these methods assume a fixed grouping of patches throughout the iterations, whereas Plug-and-Play ADMM allows re-calculation of the grouping at every iteration. In this aspect, the Plug-and-Play ADMM is a generalization of these algorithms.

A large number of denoisers we use nowadays are patch-based denoising algorithms. All these methods can be considered as variations of the class of universal denoisers [30], [31] which are asymptotically optimal and do not assume external knowledge of the latent image (e.g., prior distribution). Asymptotic optimality of patch-based denoisers has been recognized empirically by Levin et al. [32], [33], who showed that non-local means [34] approaches to the MMSE estimate as the number of patches grows to infinity. Recently, Ma et al. [35] made attempts to integrate universal denoisers with approximate message passing algorithms.

E. Contributions

The objective of this paper is to address the first and the third issue mentioned in Section I-C. The contributions of this paper are as follows:

First, we modify the original Plug-and-Play ADMM by incorporating a continuation scheme. We show that the new algorithm is guaranteed to converge for a broad class of denoisers known as the *bounded denoisers*. Boundedness is a weak assumption on the denoising algorithms which we expect most, if not all, denoisers to have. This is significantly weaker than the original method presented in [15], which requires the denoisers to be non-expansive and have symmetric gradients [13]. However, for weaker denoisers we should also expect a weaker form of convergence. We prove that the new Plug-and-Play ADMM has a *fixed point* convergence, which complements the global convergence results presented in [13].

Second, we discuss fast implementation techniques for single image super-resolution and quantized Poisson recovery problems. Unlike conventional ADMM implementations which require multiple variable splits or the use of inner iterative solvers, we propose a polyphase decomposition based method which has closed-form solutions. Consequently, we enable significantly faster realization of the Plug-and-Play ADMM framework without changing the structure.

The rest of the paper is organized as follows. We first discuss the Plug-and-Play ADMM algorithm and the convergence properties in Section II. We then discuss the applications in Section III. Experimental results are presented in Section IV.

II. PLUG-AND-PLAY ADMM AND CONVERGENCE

In this section we present the proposed Plug-and-Play ADMM and discuss its convergence property. Without loss of generality we assume $0 \leq \mathbf{x} \leq 1$.

A. Plug-and-Play ADMM

The proposed Plug-and-Play ADMM algorithm is a small change from the ADMM algorithm we presented in (5)-(7). Instead of choosing a constant ρ , we increase ρ by $\rho_{k+1} = \gamma_k \rho_k$ for $\gamma_k \geq 1$. In optimization literature, this is known as a continuation scheme [36] and has been used in various problems, e.g., [37], [38]. Incorporating this idea into the ADMM algorithm, we obtain the following iteration:

$$\mathbf{x}^{(k+1)} = \underset{\mathbf{x}}{\operatorname{argmin}} f(\mathbf{x}) + (\rho_k/2) \|\mathbf{x} - (\mathbf{v}^{(k)} - \mathbf{u}^{(k)})\|^2 \quad (10)$$

$$\mathbf{v}^{(k+1)} = \mathcal{D}_{\sigma_k}(\mathbf{x}^{(k+1)} + \mathbf{u}^{(k)}) \quad (11)$$

$$\mathbf{u}^{(k+1)} = \mathbf{u}^{(k)} + (\mathbf{x}^{(k+1)} - \mathbf{v}^{(k+1)}) \quad (12)$$

$$\rho_{k+1} = \gamma_k \rho_k, \quad (13)$$

where \mathcal{D}_{σ_k} is a denoising algorithm (called a ‘‘denoiser’’ for short), and $\sigma_k \stackrel{\text{def}}{=} \sqrt{\lambda/\rho_k}$ is a parameter controlling the strength of the denoiser.

There are different possibilities in setting γ_k . In this paper we present two options. The first one is a *constant update* rule which defines

$$\gamma_k = \gamma, \quad \text{for all } k \quad (14)$$

for a constant $\gamma > 1$. The second option is an *adaptive update* rule by considering the relative residue:

$$\Delta_{k+1} \stackrel{\text{def}}{=} \frac{1}{\sqrt{n}} \left(\|\mathbf{x}^{(k+1)} - \mathbf{x}^{(k)}\|_2 + \|\mathbf{v}^{(k+1)} - \mathbf{v}^{(k)}\|_2 + \|\mathbf{u}^{(k+1)} - \mathbf{u}^{(k)}\|_2 \right). \quad (15)$$

For any $\eta \in [0, 1)$ and let $\gamma > 1$ be a constant, we conditionally choose γ_k according to the followings:

- If $\Delta_{k+1} \geq \eta \Delta_k$, then $\gamma_k = \gamma$.
- If $\Delta_{k+1} < \eta \Delta_k$, then $\gamma_k = 1$.

The adaptive update scheme is inspired from [39], which was originally used to accelerate ADMM algorithms for strongly and weakly convex problems. Note that the constant update is a special case of the adaptive update when $\eta = 0$. Algorithm 1 shows the overall Plug-and-Play ADMM.

Algorithm 1 Plug-and-Play ADMM

Input: $\rho_0, \lambda, \eta < 1, \gamma > 1$.

while Not Converge **do**

$$\mathbf{x}^{(k+1)} = \underset{\mathbf{x}}{\operatorname{argmin}} f(\mathbf{x}) + (\rho_k/2) \|\mathbf{x} - (\mathbf{v}^{(k)} - \mathbf{u}^{(k)})\|^2$$

$$\mathbf{v}^{(k+1)} = \mathcal{D}_{\sigma_k}(\mathbf{x}^{(k+1)} + \mathbf{u}^{(k)}), \text{ where } \sigma_k = \sqrt{\lambda/\rho_k}$$

$$\mathbf{u}^{(k+1)} = \mathbf{u}^{(k)} + (\mathbf{x}^{(k+1)} - \mathbf{v}^{(k+1)})$$

if $\Delta_{k+1} \geq \eta \Delta_k$ **then**

$$\rho_{k+1} = \gamma \rho_k$$

else

$$\rho_{k+1} = \rho_k$$

end if

$$k = k + 1.$$

end while

Remark 1 (Comparison with [15]): In the original Plug-and-Play ADMM by Venkatakrishnan et al. [15], the update scheme for ρ_k was not included, i.e., $\rho_k = \rho$ for some constant ρ . This is valid, in fact better, when the denoiser \mathcal{D}_σ is non-expansive and has symmetric gradient. However, for general denoisers which could be expansive, the update scheme for ρ_k becomes crucial to the convergence. (See discussion about non-expansiveness in Section II-B.)

Remark 2 (Role of σ_k): Many denoising algorithms nowadays such as BM3D and non-local means require one major parameter¹, typically an estimate of the noise level, to control the strength of the denoiser. In our algorithm, the parameter σ_k in (11) is reminiscent to the noise level in that respect. However, unlike BM3D and non-local means where σ_k reflects the standard deviation of the i.i.d. Gaussian noise, in Plug-and-Play ADMM the residue $(\mathbf{v} - \tilde{\mathbf{v}}^{(k)})$ at the k th iterate is not Gaussian. Theoretically, we have to find a non-Gaussian denoiser but practically this could be even harder than solving the original problem. Thus two solutions have been proposed in the literature. The first one is the denoise-AMP method [23] which utilizes the random nature of the matrix \mathbf{A} in $f(\mathbf{x}) = \|\mathbf{A}\mathbf{x} - \mathbf{y}\|^2$ so that all residue is i.i.d. Gaussian according to central limit theorem. The second one is the original Plug-and-Play ADMM [13] which enforces non-expansiveness of the denoiser so that the Gaussian requirement becomes irrelevant. The proposed Plug-and-Play ADMM has the same spirit as [13] with a slight difference that we relax the global optimality criteria to a fixed point criteria. As will be demonstrated in the later part of this paper, giving up global optimality does not mean that we will obtain worse PSNR. It only means that we lose a certificate to claim whether the algorithm has converged to the global optimal of certain objective function. In practice, landing on a fixed point can give similar or sometimes better results in terms of PSNR.

B. Global and Fixed Point Convergence

Before we discuss the convergence behavior, we must clarify the type of convergence we should expect.

¹A denoising algorithm often involves a number of *internal* parameters. However, as these internal parameters do not have direct interaction with the ADMM algorithm, in this paper we keep all internal parameters in their default settings to simplify the analysis.

We refer to the type of convergence in the conventional ADMM as *global convergence*, i.e., convergence in primal residue, primal objective and dual variables. To ensure global convergence, one sufficient condition is that g is convex, proper and closed [14]. However, seeking global convergence is difficult for Plug-and-Play ADMM because for an arbitrary \mathcal{D}_σ , it is not always possible to find a convex, proper and closed g which satisfies (8) and (9). Indeed, it is possible that \mathcal{D}_σ is a solution of a variational inequality, yet there may not exist a corresponding optimization [40].

To show the existence of g , Sreehari et al. [13] propose a sufficient condition that \mathcal{D}_σ has to have symmetric gradient and is non-expansive. In this case, g exists due to a proximal mapping theorem of Moreau [41]. However, proving non-expansive denoisers could be difficult as it requires

$$\|\mathcal{D}_\sigma(\mathbf{x}) - \mathcal{D}_\sigma(\mathbf{y})\|^2 \leq \kappa \|\mathbf{x} - \mathbf{y}\|^2$$

for any \mathbf{x} and \mathbf{y} , with $\kappa \leq 1$. Even for algorithms as simple as non-local means, one can verify numerically that there exists pairs (\mathbf{x}, \mathbf{y}) that would cause $\kappa > 1$. In the Appendix we demonstrate a counter example.

Since \mathcal{D}_σ is arbitrary (or at most bounded in this paper) and we do not even know the existence of g , it is unrealistic to ask for global convergence. Therefore, what we will do in this paper is to consider fixed point convergence. Fixed point convergence guarantees that a nonlinear algorithm can enter into a steady state asymptotically. In nonlinear dynamical systems, these limit points are referred to as the stable-fixed-points and for any initial guess lying in a region called the basin of attraction the algorithm will converge [42]. For Plug-and-Play ADMM, it is reasonable to conjecture that fixed point convergence is the best we can ask for. Moving any step further will likely require additional assumptions on the denoiser \mathcal{D}_σ and its corresponding regularization g .

C. Convergence Analysis of Plug-and-Play ADMM

To begin our discussion of the convergence of Plug-and-Play ADMM, we first define the class of bounded denoisers.

Definition 1: (Bounded Denoiser). A *bounded denoiser* with a finite denoising parameter σ is a function $\mathcal{D}_\sigma : [0, 1]^n \rightarrow [0, 1]^n$ such that for any input $\mathbf{x} \in [0, 1]^n$,

$$\|\mathcal{D}_\sigma(\mathbf{x}) - \mathbf{x}\|^2/n \leq \sigma^2 C, \quad (16)$$

for some universal constant $C < \infty$ independent of \mathbf{x} and σ .

Condition (16) is mild and we expect most denoisers to hold. It suggests that when applying \mathcal{D}_σ to a noisy image \mathbf{x} , the output $\mathcal{D}_\sigma(\mathbf{x})$ must be bounded. As a special case when $\sigma = 0$, the denoiser becomes identity, i.e., $\mathcal{D}_\sigma(\mathbf{x}) = \mathbf{x}$. When this happens, the upper bound σC becomes tight. We do not consider the case when $\sigma \rightarrow \infty$, because for the sequence of ρ_k defined in (13), $\sigma_k \stackrel{\text{def}}{=} \sqrt{\lambda/\rho_k} \rightarrow 0$ as $\rho_k \rightarrow \infty$.

Remark 3: It is instructive to compare a bounded denoiser with a ‘‘proper denoiser’’ defined in [23]. A proper denoiser $\tilde{\mathcal{D}}_\sigma$ is a mapping that denoises a noisy input $\mathbf{x} + \sigma\epsilon$ with the property that

$$\mathbb{E} \left[\|\tilde{\mathcal{D}}_\sigma(\mathbf{x} + \sigma\epsilon) - \mathbf{x}\|^2/n \right] \leq \kappa\sigma^2, \quad (17)$$

for any $\kappa < 1$, where $\epsilon \sim \mathcal{N}(0, \mathbf{I})$ is the i.i.d. Gaussian noise. For large n , we can ignore the expectation because the left hand side of (17) is very likely to be concentrated around its mean. In this case, it is not difficult to see that any denoiser satisfying (17) will automatically satisfy (16). Thus, the set of bounded denoisers is broader than the set of proper denoisers. However, a bounded denoiser has weaker denoising capability than a proper denoiser because it does not explicitly reduce the i.i.d. Gaussian noise as in the proper denoiser. It only guarantees that the denoised output does not grow indefinitely. The advantage, however, is that a bounded denoiser is applicable regardless of the noise type. This makes the Plug-and-Play ADMM more flexible.

Besides the conditions on \mathcal{D}_σ we also assume that the negative log-likelihood function f has bounded gradients:

Assumption 1: We assume that $f : [0, 1]^n \rightarrow \mathbb{R}$ has bounded gradients. That is, for any $\mathbf{x} \in [0, 1]^n$, there exists $L < \infty$ such that $\|\nabla f(\mathbf{x})\|_2/\sqrt{n} \leq L$.

Example 1: Let $f(\mathbf{x}) = \|\mathbf{A}\mathbf{x} - \mathbf{y}\|_2^2$ for $\mathbf{A} \in \mathbb{R}^{n \times n}$ with eigenvalues bounded between 0 and 1. Thus, for any $\mathbf{x} \in [0, 1]^n$, we also have $\mathbf{y} \in [0, 1]^n$. The gradient of f is $\nabla f(\mathbf{x}) = 2\mathbf{A}^T(\mathbf{A}\mathbf{x} - \mathbf{y})$ and

$$\begin{aligned} \|\nabla f(\mathbf{x})\|_2/\sqrt{n} &\leq (2\lambda_{\max}(\mathbf{A})^2 \|\mathbf{x}\|_2 + 2\lambda_{\max}(\mathbf{A}) \|\mathbf{y}\|_2)/\sqrt{n} \\ &\leq 2(\|\mathbf{x}\|_2 + \|\mathbf{y}\|_2)/\sqrt{n} \leq 4, \end{aligned}$$

where the last inequality holds because $\|\mathbf{x}\|_2 \leq \sqrt{n}$ for any $\mathbf{x} \in [0, 1]^n$.

The main convergence result of this paper is as follows.

Theorem 1: (Fixed Point Convergence of Plug-and-Play ADMM). Under Assumption 1 and for any bounded denoiser \mathcal{D}_σ , the iterates of the Plug-and-Play ADMM defined in Algorithm 1 demonstrates a fixed-point convergence. That is, there exists $(\mathbf{x}^*, \mathbf{v}^*, \mathbf{u}^*)$ such that $\|\mathbf{x}^{(k)} - \mathbf{x}^*\|_2 \rightarrow 0$, $\|\mathbf{v}^{(k)} - \mathbf{v}^*\|_2 \rightarrow 0$ and $\|\mathbf{u}^{(k)} - \mathbf{u}^*\|_2 \rightarrow 0$ as $k \rightarrow \infty$.

Proof: See Appendix B. ■

Intuitively, what Theorem 1 shows is that since f and \mathcal{D}_σ are both bounded, by forcing $\rho_k \rightarrow \infty$, the inversion in (10) and the denoising in (11) have reducing influence as ρ_k grows. Consequently, the algorithm converges to a fixed point.

D. Stopping Criteria, Internal Parameters, Initial Point

We now present additional details about the algorithm in terms of stopping criteria, internal parameters and initial point.

Since we are seeking for fixed point convergence, a natural stopping criteria is to determine if $\|\mathbf{x}^{(k+1)} - \mathbf{x}^{(k)}\|_2$, $\|\mathbf{v}^{(k+1)} - \mathbf{v}^{(k)}\|_2$ and $\|\mathbf{u}^{(k+1)} - \mathbf{u}^{(k)}\|_2$ are sufficiently small. Following the definition of Δ_{k+1} in (15), we choose to terminate the iteration when

$$\begin{aligned} \Delta_{k+1} \stackrel{\text{def}}{=} \frac{1}{\sqrt{n}} \left(\|\mathbf{x}^{(k+1)} - \mathbf{x}^{(k)}\|_2 + \|\mathbf{v}^{(k+1)} - \mathbf{v}^{(k)}\|_2 \right. \\ \left. + \|\mathbf{u}^{(k+1)} - \mathbf{u}^{(k)}\|_2 \right) \leq \text{tol} \end{aligned} \quad (18)$$

for some tolerance level tol . Alternatively, we can also terminate the algorithm when

$$\max \{ \epsilon_1, \epsilon_2, \epsilon_3 \} \leq \text{tol}/3,$$

where $\epsilon_1 = \|\mathbf{x}^{(k+1)} - \mathbf{x}^{(k)}\|_2 / \sqrt{n}$, $\epsilon_2 = \|\mathbf{v}^{(k+1)} - \mathbf{v}^{(k)}\|_2 / \sqrt{n}$ and $\epsilon_3 = \|\mathbf{u}^{(k+1)} - \mathbf{u}^{(k)}\|_2 / \sqrt{n}$.

In practice, the tolerance level does not need to be extremely small in order to achieve good reconstruction quality. In fact, for many images we have tested, setting $\text{tol} \approx 10^{-3}$ is often sufficient. Figure 1 provides a justification. In this experiment, we tested an image super-resolution problem for 10 testing images (See Configuration 3 in Section IV-A for details). It can be observed that the PSNR becomes steady when tol drops below 10^{-3} . Moreover, size of the image does not seem to be an influencing factor. Smaller images such as Cameraman256, House256 and Peppers256 shows similar characteristics as bigger images. The more influencing factor is the combination of the update ratio γ and the initial value ρ_0 . However, unless γ is close to 1 and ρ_0 is extremely small (which does not yield good reconstruction anyway), our experience is that setting tol at 10^{-3} is usually valid for $\gamma \in (1, 2)$ and $\rho_0 \in (10^{-4}, 10^{-2})$.

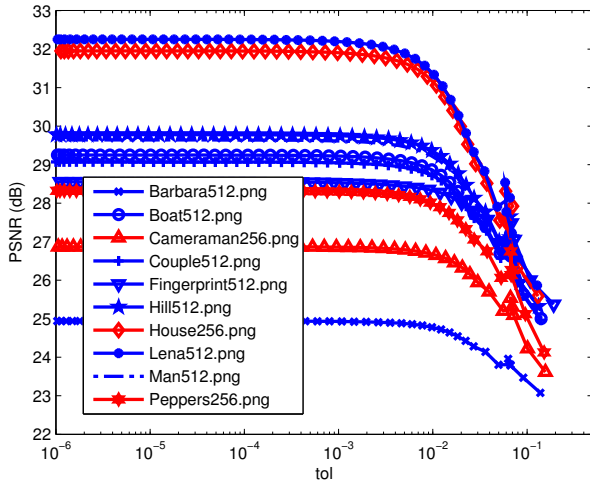


Fig. 1: Stopping criteria. The PSNR drops as the tolerance level increases. However, regardless of the size of the images, the PSNR becomes steady when $\text{tol} \approx 10^{-3}$.

The choice of the initial parameter ρ_0 requires some tuning but is typically good for $\rho_0 \in (10^{-4}, 10^{-2})$. This is in big contrast to the original Plug-and-Play ADMM [13] which requires a highly precise ρ_0 . For example, in Figure 2 we show the result of the same super-resolution experiment. We tested different values of ρ_0 , ranging from 10^0 to 10^{-4} , for the original Plug-and-Play ADMM (i.e., with constant $\rho_k = \rho_0$, the red lines), constant update rule (i.e., $\rho_{k+1} = \gamma\rho_k$, the blue lines), and the adaptive update rule (i.e., update ρ_k when Δ_{k+1} is large, the black lines). The results indicate that for the same range of ρ_0 , the constant update (blue) and the adaptive update (black) have significantly less variations in the limiting point than the original Play-and-Play ADMM. For example, the original Play-and-Play ADMM requires a precise $\rho_0 = 1$ to achieve the best PSNR. When ρ_0 is less than 10^{-2} , the final PSNR becomes very poor. In contrast, the update rules allow a much wider range of ρ_0 to achieve similar PSNR. The only caution is that ρ_0 should not be too large, for otherwise the algorithm will enter steady state early. As for which update

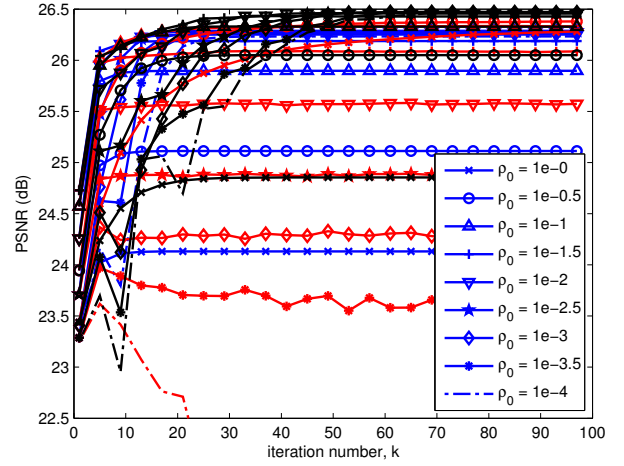


Fig. 2: Influence of ρ_0 . Red curves represent the original method in [13]; Blue curves represent the constant update rule; Black curves represent the adaptive update rule. Note the diversified behavior of the red curve, which implies that a precise ρ_0 is required. The blue and black curves are more robust.

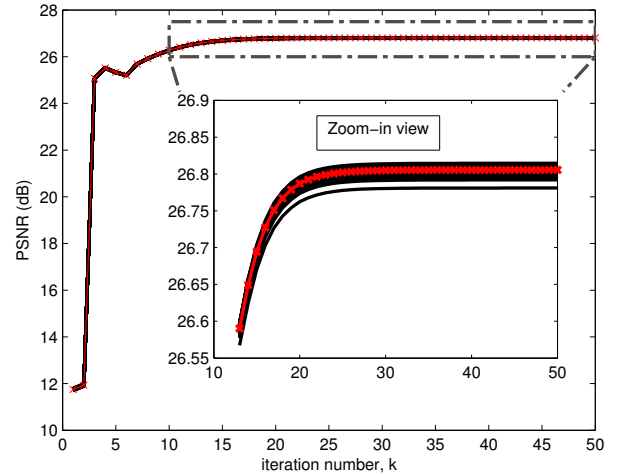


Fig. 3: Influence of the initial point $\mathbf{x}^{(0)}$. We start the algorithm with 100 different initial guesses $\mathbf{x}^{(0)}$ where each is a uniformly random vector drawn from $[0, 1]^n$. Over these 100 random realizations we plot the average. Note the small fluctuation of the PSNR at the limit.

rule should be used, there is no obvious rule of thumb to suggest under what conditions one is preferred over the other. However, experimentally we find that their difference in terms of PSNR is actually quite small.

The initial guesses $\mathbf{x}^{(0)}$, $\mathbf{v}^{(0)}$ and $\mathbf{u}^{(0)}$ have less impact to the final PSNR. This can be seen from Figure 3. In this experiment, we randomly draw 100 initial guesses $\mathbf{x}^{(0)}$ from a uniform distribution in $[0, 1]^n$. The auxiliary variable is set as $\mathbf{v}^{(0)} = \mathbf{x}^{(0)}$, and the Lagrange multiplier $\mathbf{u}^{(0)}$ is 0. As shown in Figure 3, the initial guesses do not cause significant difference in term of PSNR at the limit. The standard deviation at the limit is 0.0059 dB, implying that with 99.7% probability (3 standard deviations) the PSNR will stay within ± 0.0176 dB from its average.

III. APPLICATIONS

In this section we discuss two applications of the Plug-and-Play ADMM algorithm, namely the single image super-resolution problem and the quantized Poisson recovery for single photon imaging. Our focus here is the fast implementation of the f -subproblem in (5).

A. Application 1: Image Super-resolution

Image super-resolution can be compactly described by a linear forward model with two operations: an anti-aliasing filter and a subsampling process. The function $f(\mathbf{x})$ is quadratic in the form

$$f(\mathbf{x}) = \|\mathbf{S}\mathbf{H}\mathbf{x} - \mathbf{y}\|^2, \quad (19)$$

where the matrix $\mathbf{H} \in \mathbb{R}^{n \times n}$ is a circulant matrix representing the convolution for anti-aliasing. The matrix $\mathbf{S} \in \mathbb{R}^{m \times n}$ is a binary sampling matrix, defined as $\mathbf{S} = \text{squeeze}(\tilde{\mathbf{S}})$, where $\tilde{\mathbf{S}}$ is an $n \times n$ matrix with $\tilde{S}_{ii} = 1$ if the i th pixel is sampled and $\tilde{S}_{ij} = 0$ for all other (i, j) . The function $\text{squeeze}(\cdot) : \mathbb{R}^{n \times n} \rightarrow \mathbb{R}^{m \times n}$ discards rows with all zeros. For imaging applications, \mathbf{S} can be the standard K -fold downsampler, or a random binary sampling mask. Under different settings of \mathbf{S} and \mathbf{H} , we will have different special cases of image reconstruction problems:

- When $\mathbf{S} = \mathbf{I}$ so that there is no sampling, we have the classical non-blind image deblurring [3], [4], [38].
- When $\mathbf{H} = \mathbf{I}$ so that there is no filtering, we have the classical image interpolation [6]–[8], [43].

By defining $\mathbf{A} \stackrel{\text{def}}{=} \mathbf{S}\mathbf{H}$ we recognize that when substituting (19) into (5), the f -subproblem becomes (we dropped the iteration number k to simplify notation)

$$\hat{\mathbf{x}} = \underset{\mathbf{x} \in \mathbb{R}^n}{\text{argmin}} \|\mathbf{A}\mathbf{x} - \mathbf{y}\|^2 + \frac{\rho}{2} \|\mathbf{x} - \tilde{\mathbf{x}}\|^2. \quad (20)$$

Consequently, the solution is the pseudo-inverse

$$\hat{\mathbf{x}} = (\mathbf{A}^T \mathbf{A} + \rho \mathbf{I})^{-1} (\mathbf{A}^T \mathbf{y} + \rho \tilde{\mathbf{x}}). \quad (21)$$

For non-blind image deblurring and image inpainting, (21) has known efficient implementation as follows.

Example 2 (Non-blind deblurring): In non-blind deblurring, \mathbf{H} is circulant and so it is diagonalizable by the discrete Fourier transform matrices. Thus, (21) can be efficiently implemented using the Fourier transforms, leading to

$$\hat{\mathbf{x}} = \mathcal{F}^{-1} \left\{ \frac{\overline{\mathcal{F}(h)} \mathcal{F}(\mathbf{y}) + \rho \mathcal{F}(\tilde{\mathbf{x}})}{|\mathcal{F}(h)|^2 + \rho} \right\}, \quad (22)$$

where $\mathcal{F}(\cdot)$ is the Fourier transform operator, h is the finite impulse response filter representing the blur kernel, $\overline{(\cdot)}$ is the complex conjugate, and the multiplication/division are elementwise operations.

Example 3 (Interpolation): In image interpolation, since $\mathbf{S}^T \mathbf{S}$ is a diagonal matrix with binary entries, (21) can be efficiently implemented using an elementwise division:

$$\hat{\mathbf{x}} = (\mathbf{S}^T \mathbf{y} + \rho \tilde{\mathbf{x}}) ./ (s + \rho), \quad (23)$$

where $s = \text{diag} \{ \mathbf{S}^T \mathbf{S} \}$.

B. Polyphase Implementation for Image Super-Resolution

When $\mathbf{A} = \mathbf{S}\mathbf{H}$, solving the f -subproblem becomes non-trivial because $\mathbf{H}^T \mathbf{S}^T \mathbf{S}\mathbf{H}$ is neither diagonal nor diagonalizable by the Fourier transform. In literature, the common wisdom is to introduce multi-variable split to bypass (21) or use an inner conjugate gradient to solve (21). However, multi-variable split requires additional Lagrange multipliers and internal parameters. It also generally leads to relatively slower convergence than if we solve the problem using a single-variable split. Inner conjugate gradient does not have the problem of multi-variable split, but it is computationally expensive. In what follows, we show that when \mathbf{S} is the standard K -fold downsampler (i.e., sub-sample the spatial grid uniformly with a factor K along horizontal and vertical directions), it is possible to derive a closed-form solution.

To begin with, we note that the solution of the f -subproblem is

$$\hat{\mathbf{x}} = (\mathbf{G}^T \mathbf{G} + \rho \mathbf{I})^{-1} (\mathbf{G}^T \mathbf{y} + \rho \tilde{\mathbf{x}}), \quad (24)$$

where we defined $\mathbf{G} \stackrel{\text{def}}{=} \mathbf{S}\mathbf{H}$. Using the Sherman-Morrison-Woodbury identity, we can rewrite (24) as

$$\hat{\mathbf{x}} = \rho^{-1} \mathbf{b} - \rho^{-1} \mathbf{G}^T (\rho \mathbf{I} + \mathbf{G}\mathbf{G}^T)^{-1} \mathbf{G}\mathbf{b}, \quad (25)$$

where $\mathbf{b} \stackrel{\text{def}}{=} \mathbf{G}^T \mathbf{y} + \rho \tilde{\mathbf{x}}$. Note that if $\mathbf{S} \in \mathbb{R}^{m \times n}$ and $\mathbf{H} \in \mathbb{R}^{n \times n}$ with $m < n$, then (25) only involves a $m \times m$ inverse, which is smaller than the $n \times n$ inverse in (24).

The more critical step is the following observation. We note that the matrix $\mathbf{G}\mathbf{G}^T$ is given by

$$\mathbf{G}\mathbf{G}^T = \mathbf{S}\mathbf{H}\mathbf{H}^T \mathbf{S}^T.$$

Since \mathbf{S} is a K -fold downsampling operator, \mathbf{S}^T is a K -fold upsampling operator. Defining $\tilde{\mathbf{H}} = \mathbf{H}\mathbf{H}^T$, which can be implemented as a convolution between the blur kernel h and its time-reversal, we observe that $\tilde{\mathbf{S}}\tilde{\mathbf{H}}\tilde{\mathbf{S}}^T$ is a “upsample-filter-downsample” sequence. This idea is illustrated in Figure 4.

We next study the polyphase decomposition [44] of Figure 4. Polyphase decomposition allows us to write

$$\tilde{H}(z) = \sum_{k=0}^{K-1} z^{-k} \tilde{H}_k(z^K), \quad (26)$$

where $\tilde{H}(z)$ is the z -transform representation of the blur matrix $\tilde{\mathbf{H}} = \mathbf{H}\mathbf{H}^T$, and $\tilde{H}_k(z^K)$ is the k th polyphase component of $\tilde{H}(z)$. Illustrating (26) using a block diagram, we show in Figure 5 the decomposed structure of Figure 4. Then, using Noble identity [44], the block diagram on the left hand side of Figure 5 becomes the one shown on the right hand side. Since for any $k > 1$, placing a delay z^{-k} between an upsampling and a downsampling operator leads to a zero, the overall system simplifies to a finite impulse response filter $\tilde{H}_0(z)$, which can be pre-computed.

We summarize this by the following proposition.

Proposition 1: The operation of $\mathbf{S}\mathbf{H}\mathbf{H}^T \mathbf{S}^T$ is equivalent to applying a finite impulse response filter $\tilde{H}_0(z)$, which is the 0th polyphase component of the filter $\mathbf{H}\mathbf{H}^T$.

Proof: See the equivalence of $\mathbf{S}\mathbf{H}\mathbf{H}^T \mathbf{S}^T$ to the right hand side of Figure 4. Apply polyphase decomposition to

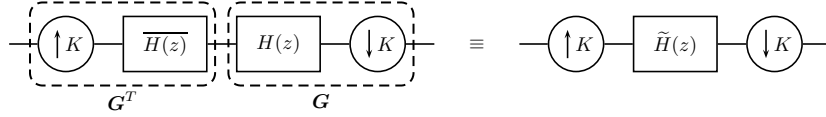


Fig. 4: [Left] Block diagram of the operation $\mathbf{G}\mathbf{G}^T$. [Right] The equivalent system, where $\tilde{H}(z) \stackrel{\text{def}}{=} \overline{H(z)}H(z)$.

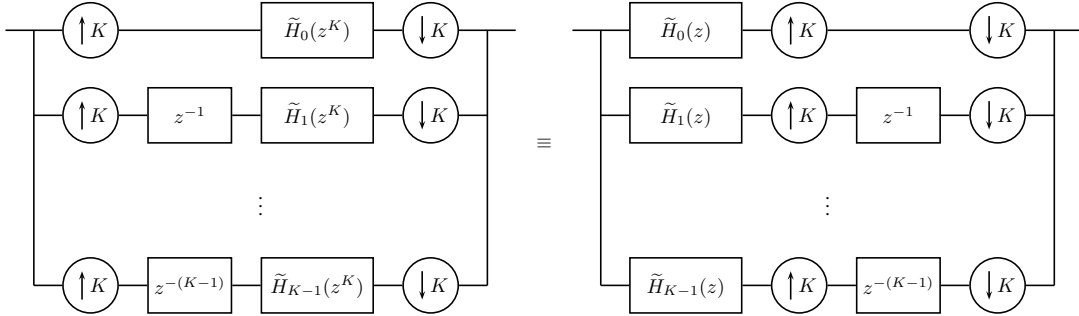


Fig. 5: [Left] Polyphase decomposition of $\tilde{H}(z)$. [Right] Equivalent representation.

Algorithm 2 Compute the 0th polyphase component.

Input: h : the blur kernel, and K : downsampling factor
 Let $\tilde{h} = \mathcal{F}^{-1}(\mathcal{F}(h)\overline{\mathcal{F}(h)})$ be the convolved filter.
 Output: $\tilde{h}_0 = (\downarrow_K)(\tilde{h})$.

Figure 4 and obtain Figure 5. Apply Noble identity to the left hand side of Figure 5. ■

To implement the 0th polyphase component, we observe that it can be done by downsampling the convolved filter $\tilde{\mathbf{H}} = \mathbf{H}\mathbf{H}^T$. This leads to the procedure illustrated in Algorithm 2.

The implication of Proposition 1 is that since $\mathbf{G}\mathbf{G}^T$ is equivalent to a finite impulse response filter \tilde{h}_0 , (25) can be implemented in closed-form using the Fourier transform:

$$\mathbf{x} = \rho^{-1}\mathbf{b} - \rho^{-1}\mathbf{G}^T \left(\mathcal{F}^{-1} \left\{ \frac{\mathcal{F}(\mathbf{G}\mathbf{b})}{|\mathcal{F}(\tilde{h}_0)|^2 + \rho} \right\} \right), \quad (27)$$

where $\mathbf{b} \stackrel{\text{def}}{=} \mathbf{G}^T \mathbf{y} + \rho \tilde{\mathbf{x}}$.

C. Application 2: Single Photon Imaging

The Plug-and-Play ADMM can be applied to Poisson problems such as Poisson denoising or Poisson deblurring [17]. In this subsection, we discuss a Poisson application which recovers images from quanta image sensors (QIS) for single photon imaging [45]–[47]. For simplicity, we will describe the problem in 1D.

QIS is a spatial oversampling device. A QIS is composed to many tiny single photon detectors called jots. In each unit space, K jots are used to acquire light corresponding to a pixel in the usual sense (e.g., a pixel in a CMOS sensor). Therefore, for an image of n pixels, a total number of nK jots are required. By assuming homogeneous distribution of the light within each pixel, we consider a simplified QIS imaging model which relates the underlying image $\mathbf{x} \in \mathbb{R}^n$ and the actual photon arrival rate at the jots $\mathbf{s} \in \mathbb{R}^{nK}$ as

$$\mathbf{s} = \mathbf{G}\mathbf{x},$$

where the matrix $\mathbf{G} \in \mathbb{R}^{nK \times n}$ is

$$\mathbf{G} = \begin{bmatrix} \mathbf{1}_{K \times 1} & \mathbf{0}_{K \times 1} & \dots & \mathbf{0}_{K \times 1} \\ \mathbf{0}_{K \times 1} & \mathbf{1}_{K \times 1} & \dots & \mathbf{0}_{K \times 1} \\ \vdots & \vdots & \ddots & \vdots \\ \mathbf{0}_{K \times 1} & \mathbf{0}_{K \times 1} & \dots & \mathbf{1}_{K \times 1} \end{bmatrix}. \quad (28)$$

Given \mathbf{s} , the photons arriving at the sensors follow a Poisson distribution with a rate given by \mathbf{s} . Let Z_i be the random variable denoting the number of photons at jot i , we have

$$p(z_i) = \frac{s_i^{-z_i} e^{-s_i}}{z_i!}, \quad i = 1, \dots, nK. \quad (29)$$

The final QIS output, Y_i , is a binary bit resulted from truncating Z_i using a threshold q . That is,

$$Y_i = \begin{cases} 1, & \text{if } Z_i \geq q, \\ 0, & \text{if } Z_i < q. \end{cases}$$

When $q = 1$, the probability of observing $Y_i = y_i$ given s_i is

$$p(y_i | s_i) = \begin{cases} e^{-s_i}, & \text{if } y_i = 0, \\ 1 - e^{-s_i}, & \text{if } y_i = 1. \end{cases}$$

The recovery goal is to estimate \mathbf{x} from the observed binary bits \mathbf{y} . Taking the negative log and summing over all pixels, the function f is defined as

$$\begin{aligned} f(\mathbf{x}) &\stackrel{\text{def}}{=} p(\mathbf{y} | \mathbf{s}) = \sum_{i=1}^{nK} -\log p(y_i | s_i) \\ &= \sum_{i=1}^{nK} -\log((1 - y_i)e^{-s_i} + y_i(1 - e^{-s_i})) \\ &= \sum_{j=1}^n -K_j^0 \log(e^{-x_j}) - K_j^1 \log(1 - e^{-x_j}), \end{aligned} \quad (30)$$

where $K_j^1 = \sum_{i=1}^K y_{(j-1)K+i}$ is the number of ones in the j th unit pixel, and $K_j^0 = \sum_{i=1}^K (1 - y_{(j-1)K+i})$ is the number of zeros in the j th unit pixel. (Note that for any j , $K_j^1 + K_j^0 = K$.) Consequently, substituting (30) into (10) yields the f -

subproblem

$$\min_{\mathbf{x}} \sum_{j=1}^n -K_j^0 \log(e^{-x_j}) - K_j^1 \log(1 - e^{-x_j}) + \frac{\rho}{2}(x_j - \tilde{x}_j)^2. \quad (31)$$

Since this optimization is separable, we can solve each individual variable x_j independently. Thus, for every j , we solve a single-variable optimization by taking derivative with respect to x_j and setting to zero, yielding

$$e^{-x_j}(K + \rho(x_j - \tilde{x}_j)) = K_j^0 + \rho(x_j - \tilde{x}_j),$$

which is a 1-dimensional root finding problem. By constructing an offline lookup table in terms of K_0 , ρ and \tilde{x}_j , we can solve (31) efficiently.

IV. EXPERIMENTAL RESULTS

In this section we present the experimental results. For consistency we use BM3D in all experiments, although other bounded denoisers will also work. We shall not compare Plug-and-Play ADMM using different denoisers as it is not the focus of the paper.

A. Image Super-Resolution

We consider a set of 10 standard test images for this experiment as shown in Figure 6. All images are gray-scaled, with sizes between 256×256 and 512×512 . We study the algorithm's performance by considering three factors in a super-resolution forward model, namely the downsampling factor K , the anti-aliasing filter \mathbf{H} , and the standard deviation of the i.i.d. Gaussian noise σ . Four sets of experimental configurations are studied, and are shown in Table I. The first two configurations are widely used in practice, whereas the latter two configurations can test the ability of the algorithm in harder situations.



Fig. 6: 10 testing images for the experiment.

TABLE I: Configurations of Super-Resolution Experiment.

Config	Description
1	$K = 2$, $\mathbf{H} = \text{bicubic}$, Noise = 0
2	$K = 4$, $\mathbf{H} = \text{bicubic}$, Noise = 0
3	$K = 2$, $\mathbf{H} = \text{Gaussian of std 1}$, Noise = 5/255
4	$K = 4$, $\mathbf{H} = \text{Gaussian of std 1}$, Noise = 5/255

We compared the proposed algorithm with several existing super-resolution algorithms. These methods include the deep convolutional neural network method (DCNN) by Dong et al. [9], the statistical patch-based sparse representation method (SPSR) by Peleg and Elad [10], the transformed self-exemplar

method (TSE) by Huang et al. [48], the classical sparse representation method for super-resolution (SR) by Yang et al. [12], and the Gaussian process regression method (GPR) by He and Siu [11]. Among these methods, we note that TSE and GPR are single image methods whereas DCNN, SPSR and SR require training using external databases. As a comparison, Plug-and-Play ADMM is a single image method.

The results of the experiment are shown in Table II. For the proposed algorithm, we optimize the parameters $(\rho_0, \gamma, \lambda)$ for each configuration. We present the two update rules as Ours-C (for constant update rule), and Ours-A (for adaptive update rule). When noise is present in the simulation, we conduct a Monte-Carlo simulation over 5 random realizations. In this case, the reported PSNR values are the average over the random realizations. The per image standard deviation is reported in the last column of Table II (if applicable).

For configurations 3 and 4 when we use a Gaussian anti-aliasing filter, we observe that not all existing methods can handle such case as the training part of those algorithms was performed on a bicubic model. Therefore, for fair comparison, we present two versions of the proposed algorithm. The first version Ours-C assumes the correct knowledge about the Gaussian filter, whereas the second version Ours-C* ignores such assumption and use the bicubic model for reconstruction.

From the PSNR results shown in Table II, we observe very similar performance of the competing methods. For configurations 1 and 2, the proposed algorithm shows the best performance overall, although in some occasions the deep neural network [9] is better. For configurations 3 and 4, we observe a significant gap between Ours-C and the competing methods. This is caused by the model mismatch of the competing methods as the implementations provided by the authors only support the bicubic model. For fairness, we consider Ours-C* by pretending that the anti-aliasing filter is bicubic. In this case, Ours-C* still performs better than the others for configuration 3, but slightly worse than GPR [11] for configuration 4.

For visual comparison we conduct a color image experiment. In this experiment, we simulate a low resolution image by downsampling the color image by a factor 4 using a bicubic anti-aliasing filter. Then, we apply the proposed algorithm to the three color channels individually to recover the image. The result is shown in Figure 7. As seen, the proposed method produces better results than SPSR [10], TSE [48] and GPR [11], with slightly sharper edges and less halo artifacts. We also observe that the deep neural network [9] shows better results than that in Table II. One possibility is that the training data used to train the neural network are natural images that have better correlation to Figure 7. However, considering the training-free nature of the proposed Plug-and-Play algorithm, losing to a well-trained neural network is not surprising.

B. Single Photon Imaging

We next consider the single-photon imaging problem. In this experiment, we note that the dominating factor is the oversampling ratio K . Therefore, we consider four sets of experiments: $K = 4, 6, 8, 10$ to test the algorithm. For comparison, we choose the two existing algorithms. The first one is

TABLE II: Image Super Resolution Results. When noise is present, the PSNR values are averaged over 5 random realizations of the noise pattern.

Size	Images										Dataset Avg	Avg STD per image
	1 512 ²	2 512 ²	3 256 ²	4 512 ²	5 512 ²	6 512 ²	7 256 ²	8 512 ²	9 512 ²	10 256 ²		
Factor: $\times 2$; Anti-aliasing Filter: Bicubic; Noise: 0												
DCNN [9]	25.71	31.83	28.79	31.13	32.73	32.60	35.11	36.34	33.10	33.05	32.04	–
SR [12]	25.87	31.51	27.92	30.94	33.02	32.46	34.79	36.14	32.80	32.67	31.81	–
SPSR [10]	25.71	31.49	27.85	31.00	33.30	32.35	34.37	36.18	32.67	32.66	31.76	–
TSE [48]	25.66	31.64	28.17	31.01	32.88	32.45	34.78	36.22	32.88	33.29	31.90	–
GPR [11]	24.99	29.99	26.44	29.50	30.36	31.33	33.08	34.19	31.09	30.98	30.20	–
Ours - C	25.87	31.85	28.81	31.42	33.63	32.56	35.30	36.45	32.86	33.06	32.18	–
Ours - A	25.74	31.68	28.44	31.27	33.49	32.39	35.20	36.02	32.65	32.65	31.95	–
Factor: $\times 4$; Anti-aliasing Filter: Bicubic; Noise: 0												
DCNN [9]	23.93	26.84	23.76	26.08	24.18	28.32	29.48	30.45	28.17	27.88	26.91	–
SR [12]	23.91	26.39	23.43	26.02	24.44	28.17	29.15	30.19	27.94	27.42	26.71	–
SPSR [10]	23.90	26.49	23.42	26.02	25.11	28.14	29.22	30.24	27.85	27.62	26.80	–
TSE [48]	23.90	26.62	23.83	26.10	24.70	28.06	30.03	30.29	28.03	27.97	26.95	–
GPR [11]	23.55	25.47	22.54	25.27	22.33	27.79	27.61	28.74	26.76	25.79	25.58	–
Ours - C	23.99	26.87	23.82	26.32	25.54	28.35	30.16	30.74	28.17	28.26	27.22	–
Ours - A	23.99	26.87	23.83	26.33	25.58	28.29	30.48	30.62	28.12	28.22	27.23	–
Factor: $\times 2$; Anti-aliasing Filter: Gaussian 9×9 , $\sigma = 1$; Noise: 5/255												
DCNN [9]	23.61	26.30	23.75	26.21	23.79	27.50	27.84	28.15	27.05	26.07	26.03	0.0219
SR [12]	23.61	26.25	23.71	26.15	23.80	27.41	27.71	28.07	26.99	26.10	25.98	0.0221
SPSR [10]	23.75	26.57	23.88	26.47	23.91	27.80	28.19	28.58	27.33	26.39	26.29	0.0208
TSE [48]	23.57	26.22	23.65	26.12	23.79	27.34	27.55	28.00	26.93	26.11	25.93	0.0238
GPR [11]	23.82	26.81	23.91	26.63	24.05	28.38	29.16	29.54	27.78	26.76	26.68	0.0170
Ours - C	24.64	29.41	26.73	29.22	28.82	29.82	32.65	32.76	29.66	30.10	29.38	0.0267
Ours - C*	24.01	27.09	24.17	27.00	25.03	28.46	29.32	29.78	27.85	26.99	26.97	0.0178
Factor: $\times 4$; Anti-aliasing Filter: Gaussian 9×9 , $\sigma = 1$; Noise: 5/255												
DCNN [9]	20.72	21.30	18.91	21.68	16.10	23.39	22.33	22.99	22.46	20.23	21.01	0.0232
SR [12]	20.67	21.30	18.86	21.51	16.37	23.15	22.19	22.85	22.26	20.33	20.95	0.0212
SPSR [10]	20.85	21.58	19.18	21.85	16.59	23.52	22.42	23.05	22.53	20.50	21.21	0.0217
TSE [48]	20.59	21.24	18.80	21.49	16.40	23.14	22.21	22.78	22.21	20.30	20.92	0.0252
GPR [11]	21.55	22.68	19.90	22.77	17.70	24.57	23.51	24.37	23.63	21.35	22.20	0.0313
Ours - C	23.62	25.75	23.06	25.30	24.48	27.17	29.14	29.42	26.86	26.86	26.17	0.0223
Ours - C*	21.21	22.12	19.43	22.43	16.90	24.37	23.13	23.95	23.39	21.13	21.81	0.0253



Fig. 7: Image Super Resolution Results. [Top](from left to right). Ground truth; The low resolution input; Bicubic interpolation; DCNN [9] (24.19dB). [Bottom](from left to right). SPSR [10] (22.44dB); TSE [48] (22.80dB); GPR [11] (20.81dB); Ours-C (23.49dB).

TABLE III: Single Photon Imaging Results. The PSNR values are averaged over 8 random realizations of the photon arrivals.

Size	Images										Dataset Avg	Avg STD per image
	1 512 ²	2 512 ²	3 256 ²	4 512 ²	5 512 ²	6 512 ²	7 256 ²	8 512 ²	9 512 ²	10 256 ²		
$K = 4$												
Yang et al. [47]	14.80	14.18	14.68	14.39	14.28	14.90	14.21	14.48	14.78	14.59	14.53	0.0157
Chan-Lu [46]	22.59	24.76	23.63	24.74	21.47	25.65	25.38	26.42	25.35	24.78	24.48	0.0425
Ours-C	25.99	25.72	25.58	26.03	23.54	26.60	28.15	28.17	26.17	26.10	26.20	0.0821
Ours-A	26.06	25.75	25.64	26.10	23.59	26.66	28.27	28.27	26.18	26.16	26.27	0.0801
$K = 6$												
Yang et al. [47]	17.94	17.27	17.67	17.61	17.29	18.22	17.22	17.62	18.00	17.65	17.65	0.0147
Chan-Lu [46]	23.97	26.25	25.53	26.26	24.47	26.66	26.75	27.32	26.58	26.40	26.02	0.0339
Ours-C	28.34	27.76	27.60	27.91	25.66	28.30	30.34	30.06	27.75	28.15	28.19	0.0451
Ours-A	28.34	27.72	27.61	27.84	25.62	28.25	30.28	29.86	27.71	28.16	28.14	0.0472
$K = 8$												
Yang et al. [47]	20.28	19.68	20.00	20.05	19.53	20.64	19.49	19.99	20.42	19.97	20.01	0.0183
Chan-Lu [46]	25.14	27.09	26.56	27.24	25.75	27.55	27.17	27.89	27.49	27.07	26.90	0.0325
Ours-C	29.79	29.07	29.14	29.25	27.19	29.55	31.70	31.43	28.99	29.52	29.56	0.0527
Ours-A	29.74	29.00	29.09	29.16	27.14	29.51	31.54	31.35	28.94	29.43	29.49	0.0520
$K = 10$												
Yang et al. [47]	22.14	21.60	21.89	21.98	21.32	22.51	21.32	21.86	22.35	21.83	21.88	0.0198
Chan-Lu [46]	26.20	27.57	27.26	27.70	26.41	27.99	27.64	28.16	27.95	27.66	27.46	0.0264
Ours-C	30.88	30.19	30.34	30.31	28.29	30.48	32.68	32.29	29.97	30.56	30.60	0.0386
Ours-A	30.81	30.12	30.31	30.22	28.22	30.41	32.51	32.17	29.90	30.47	30.51	0.0397

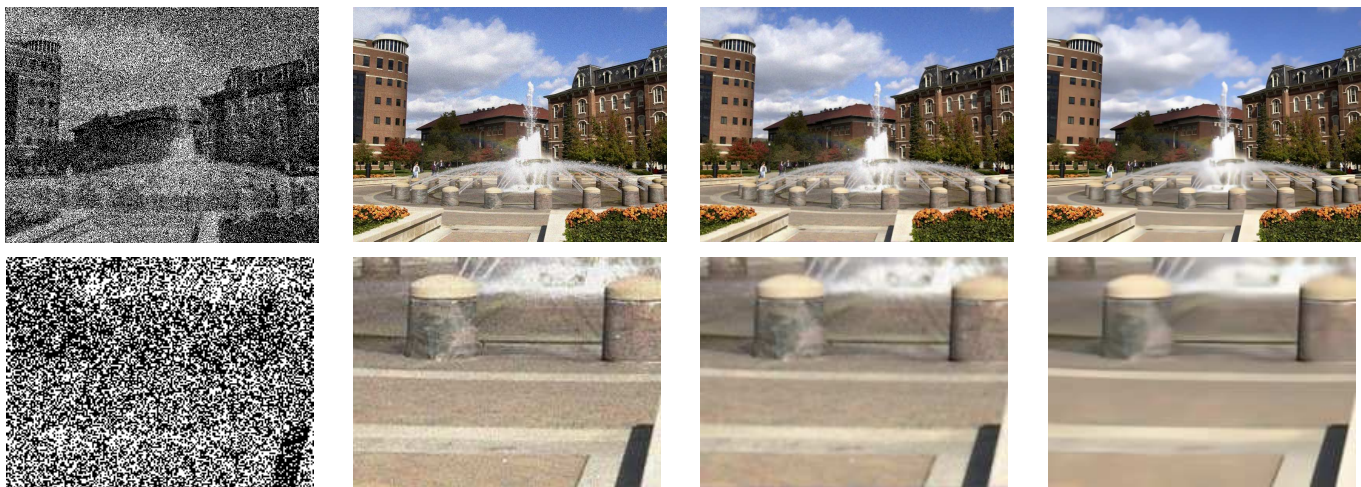


Fig. 8: Single photon imaging results. Left to Right: Input binary pattern; Yang et al. [47] (20.16dB); Chan and Lu [46] (26.74dB); Ours-C (28.81dB). The bottom row is a zoomed-in figure of the top row.

the maximum likelihood estimation (MLE) method by Yang et al. [47]. For our specific choice of \mathbf{G} in (28), the MLE solution has a closed-form expression. The second method is a total variation method by Chan and Lu [46]. This method utilizes the ADMM algorithm when solving the problem. We are aware of other existing Poisson denoising methods such as [17], [37], [49]–[51]. However, none of these methods are directly applicable to the quantized Poisson problem.

For single photon imaging, the observed binary pattern is a random array according to the Poisson process of the photon arrivals. Therefore, in order to ensure the consistency of the results, we perform a Monte-Carlo simulation by repeating each case for 8 independent trials. We then report the average and the standard deviation of these 8 independent trials. As shown in Table III, the standard deviation is indeed insignificant compared to the average PSNR. Here, we report

the dataset average over the 10 images to ensure sufficient variability of the test.

To visually compare the performance, in Figure 8 we show the result of a color image. In this experiment, we process the 3 color channels individually. For each channel, we simulate the photon arrivals by assuming $K = 8$. Then, we reconstruct the image using different algorithms. The result in Figure 8 shows that visually the proposed algorithm produces images with less noise.

V. CONCLUSION

We presented a general framework called Plug-and-Play ADMM for solving inverse problems in image restoration. Plug-and-Play ADMM uses a denoiser to replace one of the steps in the conventional ADMM algorithm. By incorporating a parameter update scheme, we showed that Plug-and-Play

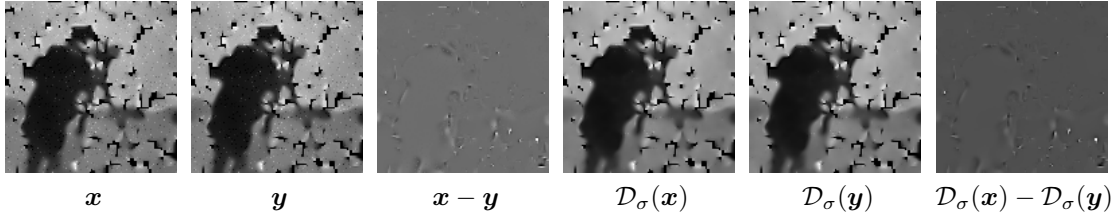


Fig. 9: Counter example showing non-local means is expansive. $\kappa = \|\mathcal{D}_\sigma(\mathbf{x}) - \mathcal{D}_\sigma(\mathbf{y})\|^2 / \|\mathbf{x} - \mathbf{y}\|^2 = 1.1775$.

ADMM is guaranteed to converge to a fixed point for any bounded denoisers. We demonstrated applications of the Plug-and-Play ADMM for two image restoration tasks, namely the single image super-resolution and the single photon imaging problem. For the single image super-resolution problem, we presented a closed-form approach to solve one of the two subproblems in the ADMM algorithm. The closed-form result allows significantly faster implementation than iterative methods. We verified the performance of the Plug-and-Play ADMM through a sequence of experiments. Plug-and-Play ADMM performs better than several existing methods, but worse than a recent neural network approach. However, the single-image nature of the Plug-and-Play ADMM makes it advantageous in situations when training is difficult.

ACKNOWLEDGEMENT

The authors thank Professor Charles Bouman and Suhas Sreehari for useful discussions.

APPENDIX A

COUNTER EXAMPLE OF NON-EXPANSIVE DENOISER

As mentioned in Section II.B, showing non-expansiveness of a denoiser could be difficult. Here we provide a counter example for the non-local means [34].

To show that non-local means are expansive, we only need to find a pair (\mathbf{x}, \mathbf{y}) such that

$$\kappa = \|\mathcal{D}_\sigma(\mathbf{x}) - \mathcal{D}_\sigma(\mathbf{y})\|^2 / \|\mathbf{x} - \mathbf{y}\|^2 > 1.$$

To construct such example, we show in Figure 9 a pair of (\mathbf{x}, \mathbf{y}) obtained through an inpainting problem using Plug-and-Play ADMM with constant ρ , i.e., $\gamma = 1$. (In fact, it does not matter how we obtain this pair of (\mathbf{x}, \mathbf{y}) . All we need to show is that there exists (\mathbf{x}, \mathbf{y}) which makes $\kappa > 1$.)

The non-local means is a weighted average operation with weights

$$W_{ij} = \exp\{-\|\mathbf{x}_i - \mathbf{x}_j\|^2 / (2\sigma^2)\},$$

where \mathbf{x}_i is the i th patch of the image \mathbf{x} . To further ensure that \mathbf{W} is doubly stochastic so that its eigenvalues are bounded between 0 and 1, we apply Sinkhorn-Knopp [52] to \mathbf{W} until convergence. Define this doubly stochastic matrix as $\widetilde{\mathbf{W}}$. Then, the denoised output is given by

$$\widetilde{\mathbf{x}} = \mathcal{D}_\sigma(\mathbf{x}) \stackrel{\text{def}}{=} \widetilde{\mathbf{W}}\mathbf{x}.$$

Therefore, the ratio we need to check is

$$\kappa = \|\widetilde{\mathbf{W}}\mathbf{x}(\mathbf{x}) - \widetilde{\mathbf{W}}\mathbf{y}(\mathbf{y})\|^2 / \|\mathbf{x} - \mathbf{y}\|^2,$$

where the subscript $(\cdot)_x$ specifies the dependency of $\widetilde{\mathbf{W}}$ on \mathbf{x} (or \mathbf{y}). The denoised results are shown in Figure 9 (c) and (d). Although it may look subtle, one can verify that $\kappa = 1.1775$ which violates the requirement of non-expansiveness. This happens because $\widetilde{\mathbf{W}}_x \neq \widetilde{\mathbf{W}}_y$ for $\mathbf{x} \neq \mathbf{y}$. The dependency on \mathbf{x} and \mathbf{y} makes the operators nonlinear, and hence makes non-expansiveness difficult to validate.

Readers at this point may wonder why the proposed Plug-and-Play ADMM can alleviate the expansive issue. In a nutshell, the reason is that we force $\rho \rightarrow \infty$ so that $\sigma \rightarrow 0$. Consequently, the weight $\mathbf{W} \rightarrow \mathbf{I}$ as $\rho \rightarrow \infty$. For the original Plug-and-Play ADMM in [15], $\mathbf{W} \rightarrow \mathbf{I}$ because ρ is fixed.

APPENDIX B

PROOF OF THEOREM 1

To simplify the notations we first define a triplet $\boldsymbol{\theta}^{(k)} \stackrel{\text{def}}{=} (\mathbf{x}^{(k)}, \mathbf{v}^{(k)}, \mathbf{u}^{(k)})$. Let Θ be the domain of $\boldsymbol{\theta}^{(k)}$ for all k . Clearly, since $0 \leq \mathbf{x}^{(k)} \leq 1$, $\mathbf{v}^{(k)}$ is closed and bounded due to the bounded denoiser \mathcal{D}_σ , $\mathbf{u}^{(k)}$ must also be closed and bounded. Consequently, Θ is a closed and bounded subset in $\mathbb{R}^{n \times 3}$. On Θ we also define a distance function $D : \Theta \times \Theta \rightarrow \mathbb{R}$ such that

$$D(\boldsymbol{\theta}^{(k)}, \boldsymbol{\theta}^{(j)}) = \frac{1}{\sqrt{n}} \left(\|\mathbf{x}^{(k)} - \mathbf{x}^{(j)}\|_2 + \|\mathbf{v}^{(k)} - \mathbf{v}^{(j)}\|_2 + \|\mathbf{u}^{(k)} - \mathbf{u}^{(j)}\|_2 \right).$$

It then follows that $\Delta_{k+1} = D(\boldsymbol{\theta}^{(k+1)}, \boldsymbol{\theta}^{(k)})$. Moreover, D satisfies the properties of a norm:

- $D(\boldsymbol{\theta}^{(k)}, \boldsymbol{\theta}^{(j)}) \geq 0$, and $D(\boldsymbol{\theta}^{(k)}, \boldsymbol{\theta}^{(j)}) = 0$ iff $j = k$.
- $D(\boldsymbol{\theta}^{(k)}, \boldsymbol{\theta}^{(j)}) = D(\boldsymbol{\theta}^{(j)}, \boldsymbol{\theta}^{(k)})$.
- $D(\boldsymbol{\theta}^{(k)}, \boldsymbol{\theta}^{(j)}) + D(\boldsymbol{\theta}^{(k)}, \boldsymbol{\theta}^{(\ell)}) \leq D(\boldsymbol{\theta}^{(j)}, \boldsymbol{\theta}^{(\ell)})$.

Therefore, (Θ, D) forms a compact metric subspace in $\mathbb{R}^{n \times 3}$ and hence all Cauchy sequences defined on (Θ, D) converges. Our goal is to show that the sequence $\{\boldsymbol{\theta}^{(k)}\}_{k=1}^\infty$ returned by the Plug-and-Play ADMM is Cauchy.

The Plug-and-Play ADMM involves two cases of the parameter update:

- Case 1: If $\Delta_{k+1} > \eta\Delta_k$, then $\rho_{k+1} = \gamma\rho_k$.
- Case 2: If $\Delta_{k+1} \leq \eta\Delta_k$, then $\rho_{k+1} = \rho_k$.

At iteration k , if Case 1 holds, then by Lemma 1, $\boldsymbol{\theta}^{(k+1)}$ satisfies

$$D(\boldsymbol{\theta}^{(k+1)}, \boldsymbol{\theta}^{(k)}) \leq \frac{C'}{\sqrt{\rho_k}}, \quad (32)$$

for some universal constant $C' > 0$ independent of k . On the other hand, if Case 2 holds, then since $\Delta_{k+1} = D(\boldsymbol{\theta}^{(k+1)}, \boldsymbol{\theta}^{(k)})$ we have

$$D(\boldsymbol{\theta}^{(k+1)}, \boldsymbol{\theta}^{(k)}) \leq \eta D(\boldsymbol{\theta}^{(k)}, \boldsymbol{\theta}^{(k-1)}). \quad (33)$$

As $k \rightarrow \infty$, one of the following three situations will happen:

- (S_1) : Case 1 occurs infinitely many times but Case 2 occurs finitely many times;
- (S_2) : Case 2 occurs infinitely many times but Case 1 occurs finitely many times;
- (S_3) : Both Case 1 and Case 2 occur infinitely many times.

When (S_1) happens, ρ_k has to be updated infinitely many times. Therefore, $\rho_k \rightarrow \infty$ as $k \rightarrow \infty$. Then by (32) $D(\boldsymbol{\theta}^{(k+1)}, \boldsymbol{\theta}^{(k)}) \rightarrow 0$. When (S_2) happens, there must exist a K such that for $k \geq K$ only Case 2 will be visited and there is no more Case 1. Thus, by induction we have

$$\begin{aligned} D(\boldsymbol{\theta}^{(k+1)}, \boldsymbol{\theta}^{(k)}) &\leq \eta^{k-K} D(\boldsymbol{\theta}^{(K)}, \boldsymbol{\theta}^{(K-1)}) \\ &\leq \eta^{k-K} \frac{C'}{\rho_{K-1}} \rightarrow 0, \end{aligned}$$

because $\eta < 1$ and ρ_{K-1} is a bounded constant. When (S_3) happens, we again have $\rho_k \rightarrow \infty$ as $k \rightarrow \infty$. Therefore, by (32), $D(\boldsymbol{\theta}^{(k+1)}, \boldsymbol{\theta}^{(k)}) \rightarrow 0$.

To summarize, we have shown that regardless which of (S_1)-(S_3), we always have

$$D(\boldsymbol{\theta}^{(k+1)}, \boldsymbol{\theta}^{(k)}) \rightarrow 0, \quad (34)$$

as $k \rightarrow \infty$. Therefore, $\{\boldsymbol{\theta}^{(k)}\}_{k=1}^{\infty}$ is a Cauchy sequence. Since a Cauchy sequence on a compact metric space (Θ, D) always converges, there must exist $\boldsymbol{\theta}^* = (\mathbf{x}^*, \mathbf{v}^*, \mathbf{u}^*)$ such that

$$D(\boldsymbol{\theta}^{(k)}, \boldsymbol{\theta}^*) \rightarrow 0. \quad (35)$$

Consequently, we have $\|\mathbf{x}^{(k)} - \mathbf{x}^*\|_2 \rightarrow 0$, $\|\mathbf{v}^{(k)} - \mathbf{v}^*\|_2 \rightarrow 0$ and $\|\mathbf{u}^{(k)} - \mathbf{u}^*\|_2 \rightarrow 0$. This completes the proof.

Lemma 1: At iteration k , if Case 1 holds, then

$$D(\boldsymbol{\theta}^{(k+1)}, \boldsymbol{\theta}^{(k)}) \leq \frac{C'}{\sqrt{\rho_k}}, \quad (36)$$

for some universal constant $C' > 0$ independent of k .

Proof: Following the definition of $D(\boldsymbol{\theta}^{(k+1)}, \boldsymbol{\theta}^{(k)})$, it is sufficient to show that

$$\begin{aligned} \frac{1}{\sqrt{n}} \|\mathbf{x}^{(k+1)} - \mathbf{x}^{(k)}\|_2 &\leq \frac{C_1}{\sqrt{\rho_k}}, \\ \frac{1}{\sqrt{n}} \|\mathbf{v}^{(k+1)} - \mathbf{v}^{(k)}\|_2 &\leq \frac{C_2}{\sqrt{\rho_k}}, \\ \frac{1}{\sqrt{n}} \|\mathbf{u}^{(k+1)} - \mathbf{u}^{(k)}\|_2 &\leq \frac{C_3}{\sqrt{\rho_k}}, \end{aligned}$$

for some universal constants C_1, C_2 and C_3 .

Let us consider

$$\mathbf{x}^{(k+1)} = \underset{\mathbf{x}}{\operatorname{argmin}} f(\mathbf{x}) + \frac{\rho_k}{2} \|\mathbf{x} - (\mathbf{v}^{(k)} - \mathbf{u}^{(k)})\|^2.$$

The first order optimality implies that

$$\mathbf{x} - (\mathbf{v}^{(k)} - \mathbf{u}^{(k)}) = -\frac{1}{\rho_k} \nabla f(\mathbf{x}).$$

Since the minimizer is $\mathbf{x} = \mathbf{x}^{(k+1)}$, substituting $\mathbf{x} = \mathbf{x}^{(k+1)}$ and using the fact that ∇f is bounded yields

$$\frac{1}{\sqrt{n}} \|\mathbf{x}^{(k+1)} - (\mathbf{v}^{(k)} - \mathbf{u}^{(k)})\|_2 = \frac{\|\nabla f(\mathbf{x})\|_2}{\rho_k \sqrt{n}} \leq \frac{L}{\rho_k}. \quad (37)$$

Next, let $\tilde{\mathbf{v}}^{(k)} = \mathbf{x}^{(k+1)} + \mathbf{u}^{(k)}$ and $\sigma_k = \sqrt{\lambda/\rho_k}$. Define

$$\mathbf{v}^{(k+1)} = \mathcal{D}_{\sigma_k}(\tilde{\mathbf{v}}^{(k)}).$$

Since \mathcal{D}_{σ_k} is a bounded denoiser, we have that

$$\begin{aligned} \frac{1}{\sqrt{n}} \|\mathbf{v}^{(k+1)} - (\mathbf{x}^{(k+1)} + \mathbf{u}^{(k)})\|_2 &= \frac{1}{\sqrt{n}} \|\mathbf{v}^{(k+1)} - \tilde{\mathbf{v}}^{(k)}\|_2 \\ &= \frac{1}{\sqrt{n}} \|\mathcal{D}_{\sigma_k}(\tilde{\mathbf{v}}^{(k)}) - \tilde{\mathbf{v}}^{(k)}\|_2 \leq \sigma_k \sqrt{C} = \frac{\sqrt{\lambda}\sqrt{C}}{\sqrt{\rho_k}}. \end{aligned} \quad (38)$$

We can now bound $\|\mathbf{v}^{(k+1)} - \mathbf{v}^{(k)}\|_2$ as follows.

$$\begin{aligned} \frac{1}{\sqrt{n}} \|\mathbf{v}^{(k+1)} - \mathbf{v}^{(k)}\|_2 &\leq \frac{1}{\sqrt{n}} \|\mathbf{v}^{(k+1)} - (\mathbf{x}^{(k+1)} + \mathbf{u}^{(k)})\|_2 \\ &\quad + \frac{1}{\sqrt{n}} \|(\mathbf{x}^{(k+1)} + \mathbf{u}^{(k)}) - \mathbf{v}^{(k)}\|_2. \end{aligned}$$

Using (37) and (38), we have

$$\begin{aligned} \frac{1}{\sqrt{n}} \|\mathbf{v}^{(k+1)} - \mathbf{v}^{(k)}\|_2 &\leq \frac{\sqrt{\lambda}\sqrt{C}}{\sqrt{\rho_k}} + \frac{L}{\rho_k} \\ &= \frac{1}{\sqrt{\rho_k}} \left(\sqrt{\lambda}\sqrt{C} + \frac{L}{\sqrt{\rho_k}} \right) \leq \frac{1}{\sqrt{\rho_k}} \left(\sqrt{\lambda}\sqrt{C} + \frac{L}{\sqrt{\rho_0}} \right). \end{aligned} \quad (39)$$

Similarly, we can show that

$$\begin{aligned} \frac{1}{\sqrt{n}} \|\mathbf{u}^{(k+1)}\|_2 &= \frac{1}{\sqrt{n}} \|\mathbf{u}^{(k)} + (\mathbf{x}^{(k+1)} - \mathbf{v}^{(k+1)})\|_2 \\ &= \frac{1}{\sqrt{n}} \|\mathbf{u}^{(k)} + \mathbf{x}^{(k+1)} - \mathcal{D}_{\sigma_k}(\tilde{\mathbf{v}}^{(k)})\|_2 \\ &= \frac{1}{\sqrt{n}} \|\mathbf{u}^{(k)} + \mathbf{x}^{(k+1)} - (\mathcal{D}_{\sigma_k}(\tilde{\mathbf{v}}^{(k)}) - \tilde{\mathbf{v}}^{(k)}) - \tilde{\mathbf{v}}^{(k)}\|_2 \\ &\stackrel{(a)}{=} \frac{1}{\sqrt{n}} \|\mathcal{D}_{\sigma_k}(\tilde{\mathbf{v}}^{(k)}) - \tilde{\mathbf{v}}^{(k)}\|_2 \leq \frac{\sqrt{\lambda}\sqrt{C}}{\sqrt{\rho_k}}, \end{aligned} \quad (40)$$

where (a) holds because $\tilde{\mathbf{v}}^{(k)} = \mathbf{u}^{(k)} + \mathbf{x}^{(k+1)}$. Thus,

$$\begin{aligned} \frac{1}{\sqrt{n}} \|\mathbf{u}^{(k+1)} - \mathbf{u}^{(k)}\|_2 &\leq \frac{1}{\sqrt{n}} \left(\|\mathbf{u}^{(k+1)}\|_2 + \|\mathbf{u}^{(k)}\|_2 \right) \\ &\leq \frac{2\sqrt{\lambda}\sqrt{C}}{\sqrt{\rho_k}}. \end{aligned}$$

Finally, since $\mathbf{u}^{(k+1)} = \mathbf{u}^{(k)} + (\mathbf{x}^{(k+1)} - \mathbf{v}^{(k+1)})$, we have

$$\begin{aligned} \frac{1}{\sqrt{n}} \|\mathbf{x}^{(k+1)} - \mathbf{x}^{(k)}\|_2 &= \frac{1}{\sqrt{n}} \left\| (\mathbf{u}^{(k+1)} - \mathbf{u}^{(k)} + \mathbf{v}^{(k+1)}) - (\mathbf{u}^{(k)} - \mathbf{u}^{(k-1)} + \mathbf{v}^{(k)}) \right\|_2 \\ &\leq \frac{1}{\sqrt{n}} \left(\|\mathbf{u}^{(k+1)} - \mathbf{u}^{(k)}\|_2 + \|\mathbf{u}^{(k)} - \mathbf{u}^{(k-1)}\|_2 \right. \\ &\quad \left. + \|\mathbf{v}^{(k+1)} - \mathbf{v}^{(k)}\|_2 \right) \\ &\leq \frac{2\sqrt{\lambda}\sqrt{C}}{\sqrt{\rho_k}} + \frac{2\sqrt{\lambda}\sqrt{C}}{\sqrt{\rho_{k-1}}} + \frac{1}{\sqrt{\rho_k}} \left(\sqrt{\lambda}\sqrt{C} + \frac{L}{\sqrt{\rho_k}} \right) \\ &\leq \left((3 + 2\sqrt{\gamma})\sqrt{\lambda}\sqrt{C} + \frac{L}{\sqrt{\rho_0}} \right) \frac{1}{\sqrt{\rho_k}}. \end{aligned} \quad (41)$$

REFERENCES

- [1] H. V. Poor, *An Introduction to Signal Detection and Estimation*, Springer, 2nd edition, 1998.

- [2] C. A. Bouman, "Model-based image processing," [Available online] <https://engineering.purdue.edu/~bouman/publications/pdf/MBIP-book.pdf>, 2015.
- [3] M. Afonso, J. Bioucas-Dias, and M. Figueiredo, "Fast image recovery using variable splitting and constrained optimization," *IEEE Trans. Image Process.*, vol. 19, no. 9, pp. 2345–2356, Apr. 2010.
- [4] S. H. Chan, R. Khoshabeh, K. B. Gibson, P. E. Gill, and T. Q. Nguyen, "An augmented Lagrangian method for total variation video restoration," *IEEE Trans. Image Process.*, vol. 20, no. 11, pp. 3097–3111, May 2011.
- [5] J. Yang, Y. Zhang, and W. Yin, "An efficient TVL1 algorithm for deblurring multichannel images corrupted by impulsive noise," *SIAM J. on Sci. Comput.*, vol. 31, no. 4, pp. 2842–2865, Jul. 2009.
- [6] J. Dahl, P. C. Hansen, S. H. Jensen, and T. L. Jensen, "Algorithms and software for total variation image reconstruction via first-order methods," *Numerical Algorithms*, vol. 53, no. 1, pp. 67–92, Jan. 2010.
- [7] D. Garcia, "Robust smoothing of gridded data in one and higher dimensions with missing values," *Comput. Statist. Data Anal.*, vol. 54, no. 4, pp. 1167–1178, Apr. 2010.
- [8] M. Zhou, H. Chen, L. Ren, G. Sapiro, L. Carin, and J. W. Paisley, "Non-parametric Bayesian dictionary learning for sparse image representations," in *Advances in Neural Information Processing Systems*, 2009, vol. 22.
- [9] C. Dong, C. C. Loy, K. He, and X. Tang, "Learning a deep convolutional network for image super-resolution," in *European Conference on Computer Vision*, Sep. 2014, pp. 184–199.
- [10] T. Peleg and M. Elad, "A statistical prediction model based on sparse representations for single image super-resolution," *IEEE Trans. Image Process.*, vol. 23, no. 6, pp. 2569–2582, Jun. 2014.
- [11] H. He and W. Siu, "Single image super-resolution using Gaussian process regression," in *Proc. IEEE Conf. Computer Vision and Pattern Recognition (CVPR)*, Jun. 2011, pp. 449–456.
- [12] J. Yang, J. Wright, T. Huang, and Y. Ma, "Image super-resolution as sparse representation of raw image patches," in *Proc. IEEE Conf. Computer Vision and Pattern Recognition (CVPR)*, Jun. 2008, pp. 1–8.
- [13] S. Sreehari, S. V. Venkatakrishnan, B. Wohlberg, L. F. Drummy, J. P. Simmons, and C. A. Bouman, "Plug-and-play priors for bright field electron tomography and sparse interpolation," Available online: <http://arxiv.org/abs/1512.07331>, Dec 2015.
- [14] S. Boyd, N. Parikh, E. Chu, B. Peleato, and J. Eckstein, "Distributed optimization and statistical learning via the alternating direction method of multipliers," *Found. Trends Mach. Learn.*, vol. 3, no. 1, pp. 1–122, Jan. 2011.
- [15] S. Venkatakrishnan, C. Bouman, and B. Wohlberg, "Plug-and-play priors for model based reconstruction," in *Proc. IEEE Global Conference on Signal and Information Processing*, 2013, pp. 945–948.
- [16] Y. Dar, A. M. Bruckstein, M. Elad, and R. Giryes, "Postprocessing of compressed images via sequential denoising," Available online: <http://arxiv.org/abs/1510.09041>, Oct. 2015.
- [17] A. Rond, R. Giryes, and M. Elad, "Poisson inverse problems by the plug-and-play scheme," Available online: <http://arxiv.org/abs/1511.02500>, Nov 2015.
- [18] M. Hong, Z.-Q. Luo, and M. Razaviyayn, "Convergence analysis of alternating direction method of multipliers for a family of nonconvex problems," Available online: <http://arxiv.org/abs/1410.1390>, Nov 2015.
- [19] P. Milanfar, "Symmetrizing smoothing filters," *SIAM Journal on Imaging Sciences*, vol. 6, no. 1, pp. 263–284, 2013.
- [20] S. H. Chan, T. Zickler, and Y. M. Lu, "Understanding symmetric smoothing filters via Gaussian mixtures," in *Proc. IEEE Intl. Conf. Image Process.*, Sep 2015.
- [21] S. H. Chan, "Algorithm-induced prior for image restoration," Available online: <http://arxiv.org/abs/1602.00715>, Feb. 2016.
- [22] P. Milanfar, "A tour of modern image filtering," *IEEE Signal Processing Magazine*, vol. 30, pp. 106–128, Jan. 2013.
- [23] C. A. Metzler, A. Maleki, and R. G. Baraniuk, "From denoising to compressed sensing," Available online: <http://arxiv.org/abs/1406.4175>, Jul. 2014.
- [24] C. A. Metzler, A. Maleki, and R. G. Baraniuk, "BM3D-AMP: A new image recovery algorithm based on BM3D denoising," in *Proc. IEEE Intl. Conf. Image Process.*, Sep. 2015, pp. 3116–3120.
- [25] J. Tan, Y. Ma, and D. Baron, "Compressive imaging via approximate message passing with wavelet-based image denoising," in *Proc. IEEE Global Conf. Signal Information Process.*, Dec 2014, pp. 424–428.
- [26] J. Tan, Y. Ma, and D. Baron, "Compressive imaging via approximate message passing with image denoising," *IEEE Trans. Signal Process.*, vol. 63, no. 8, pp. 2085–2092, Apr. 2015.
- [27] R. Neelamani, H. Choi, and R. Baraniuk, "ForWaRD: Fourier-Wavelet regularized deconvolution for ill-conditioned systems," *IEEE Trans. Signal Process.*, vol. 52, no. 2, pp. 418–433, Feb. 2004.
- [28] A. Danielyan, V. Katkovnik, and K. Egiazarian, "BM3D frames and variational image deblurring," *IEEE Trans. Image Process.*, vol. 21, no. 4, pp. 1715–1728, Aug 2012.
- [29] J. Zhang, D. Zhao, and W. Gao, "Group-based sparse representation for image restoration," *IEEE Trans. Image Process.*, vol. 23, no. 8, pp. 3336–3351, Aug. 2014.
- [30] T. Weissman, E. Ordentlich, G. Seroussi, S. Verdu, and M. J. Weinberger, "Universal discrete denoising: Known channel," *IEEE Trans. Information Theory*, vol. 51, no. 1, pp. 5–28, Jan 2005.
- [31] K. Sivaramakrishnan and T. Weissman, "A context quantization approach to universal denoising," *IEEE Trans. Signal Process.*, vol. 57, no. 6, pp. 2110–2129, Jun 2009.
- [32] A. Levin and B. Nadler, "Natural image denoising: Optimality and inherent bounds," in *Proc. IEEE Conf. Computer Vision and Pattern Recognition (CVPR)*, Jun. 2011, pp. 2833–2840.
- [33] A. Levin, B. Nadler, F. Durand, and W. Freeman, "Patch complexity, finite pixel correlations and optimal denoising," in *Proc. 12th European Conf. Computer Vision (ECCV)*, Oct. 2012, vol. 7576, pp. 73–86.
- [34] A. Buades, B. Coll, and J. Morel, "A review of image denoising algorithms, with a new one," *SIAM Multiscale Model and Simulation*, vol. 4, no. 2, pp. 490–530, 2005.
- [35] Y. Ma, J. Zhu, and Dror Baron, "Approximate message passing with universal denoising," Available online: <http://arxiv.org/abs/1506.02693>, Jun. 2015.
- [36] K.-M. Ng, *A Continuation Approach for Solving Nonlinear Optimization Problems with Discrete Variables*, Ph.D. thesis, Stanford University, 2002.
- [37] Z. T. Harmany, R. F. Marcia, and R. M. Willet, "This is SPIRAL-TAP: sparse Poisson intensity reconstruction algorithms: Theory and practice," *IEEE Trans. Image Process.*, vol. 21, no. 3, pp. 1084–1096, Sep. 2011.
- [38] Y. Wang, Y. Yang, W. Yin, and Y. Zhang, "A new alternating minimization algorithm for total variation image reconstruction," *SIAM J. Imaging Science*, vol. 1, no. 3, pp. 248–272, Aug. 2008.
- [39] T. Goldstein, B. O' Donoghue, S. Setzer, and R. Baraniuk, "Fast alternating direction optimization methods," Tech. Rep., UCLA, 2012, Available online: <ftp://ftp.math.ucla.edu/pub/camreport/cam12-35.pdf>.
- [40] F. Facchinei and J.-S. Pang, *Finite Dimensional Variational Inequalities and Complementarity Problems*, Springer, 2003.
- [41] J.-J. Moreau, "Proximité et dualité dans un espace Hilbertien," *Bulletin de la Société Mathématique de France*, vol. 93, pp. 273–299, 1965.
- [42] S. Wiggins, *Introduction to Applied Nonlinear Dynamical Systems and Chaos*, New York: Springer-Verlag, 1990.
- [43] L. Liu, S. H. Chan, and T. Q. Nguyen, "Depth reconstruction from sparse samples: representation, algorithm, and sampling," *IEEE Trans. Image Process.*, vol. 24, no. 6, pp. 1983–1996, Jun. 2015.
- [44] P. P. Vaidyanathan, *Multirate Systems and Filter Banks*, Prentice Hall, 1992.
- [45] E. R. Fossum, "The Quanta Image Sensor (QIS): Concepts and Challenges," in *Proc OSA Topical Mtg Computational Optical Sensing and Imaging*, Jul. 2011, paper JTuE1.
- [46] S. H. Chan and Y. M. Lu, "Efficient image reconstruction for gigapixel quantum image sensors," in *Proc IEEE Global Conf. on Signal and Information Processing (GlobalSIP'14)*, Dec 2014, pp. 312–316.
- [47] F. Yang, Y. M. Lu, L. Sbaiz, and M. Vetterli, "Bits from photons: Oversampled image acquisition using binary poisson statistics," *IEEE Trans. Image Process.*, vol. 21, no. 4, pp. 1421–1436, Apr. 2012.
- [48] J. Huang, A. Singh, and N. Ahuja, "Single image super-resolution using transformed self-exemplars," in *Proc. IEEE Conf. Computer Vision and Pattern Recognition (CVPR)*, Jun. 2015, pp. 5197–5206.
- [49] M. A. T. Figueiredo and J. M. Bioucas-Dias, "Restoration of Poissonian images using alternating direction optimization," *IEEE Trans. Image Process.*, vol. 19, no. 12, pp. 3133–3145, Dec. 2010.
- [50] J. Salmon, Z. Harmany, C. Deledalle, and R. Willet, "Poisson noise reduction with non-local PCA," *Journal of Mathematical Imaging and Vision*, vol. 48, no. 2, pp. 279–294, Feb. 2014.
- [51] M. Makitalo and A. Foi, "Optimal inversion of the generalized anscombe transformation for Poisson-Gaussian noise," *IEEE Trans. Image Process.*, vol. 22, no. 1, pp. 91–103, Jan. 2013.
- [52] R. Sinkhorn, "A relationship between arbitrary positive matrices and doubly stochastic matrices," *The Annals of Mathematical Statistics*, vol. 35, pp. 876–879, 1964.